Extreme Mechanics Letters 59 (2023) 101968

Contents lists available at ScienceDirect

Extreme Mechanics Letters

journal homepage: www.elsevier.com/locate/eml

Indentation and stability of woven domes

Samuel Poincloux[1], Célestin Vallat, Tian Chen[2], Tomohiko G. Sano[3], Pedro M. Reis*

École Polytechnique Fédérale de Lausanne (EPFL), Flexible Structures Laboratory, Lausanne, CH-1015, Switzerland

ARTICLE INFO

Article history:
Received 19 July 2022
Received in revised form 13 January 2023
Accepted 20 January 2023
Available online 21 January 2023

Keywords:
Discrete domes
Triaxial weaving
Indentation
Bistability

ABSTRACT

Discrete domes are doubly curved structures comprising a network of beam-like elements. We study the mechanics of discrete domes made of ribbons woven in a pentagonal triaxial pattern. Experiments and finite element simulations are performed to characterize the mechanical response of each woven dome under indentation. The observed nonlinear response features force maxima, snap-through inversion, and non-monotonic evolution, leading to additional stable configurations. The dome's rest shape can be tuned continuously by designing the in-plane curvature of the ribbons and is then perturbed by adjustable clamped boundary conditions at their extremities. These control parameters are leveraged to smoothly and selectively modify the nonlinear features of the mechanical response, including multi-stability. Finally, we suggest a simplified model based on an *elastica* approximation to predict the stability of the inverted state successfully. The strong geometrical constraints imposed by the weaving pattern and the ribbons enable us to rationalize and tune the indentation response of these intriguing discrete structures.

1. Introduction

Triaxial weaving is a traditional craft used to assemble sets of long flexible ribbons into three-dimensional (3D) curved surfaces. Initially used for basket making, this technique is of growing interest for design [1–3] and engineering [4,5] applications. A triaxial weave is typically composed of ribbons, arranged as a *kagome* lattice, with alternating over- and under-crossings in a basic pattern consisting of polygons surrounded by triangles. By modifying the number of sides of the polygons, the woven structure can adopt flat, dome, or saddle-like shapes [2]. Recently, we have uncovered a novel geometry-induced mechanism to smoothly change the shape of weaves while maintaining the topology of the underlying pattern by varying the in-plane curvature of the constituent ribbons [6]. This mechanism was then leveraged by optimizing the shape of the ribbon to inverse-design free-form and stable 3D weaves [7]. Beyond attaining desired shapes, the mechanics of 3D weaves is also of growing interest [8] and, networks of coupled ribbons are known to exhibit rich and nontrivial stability landscapes [9].

Three-dimensional weaves are reminiscent of other dome-like structures with a network of discrete beam elements, which may be linked rigidly for space frames [10,11], or buckled with rotation-free crossings for gridshells [12,13]. Such structures are used widely at the macroscopic and microscopic scales. Architecture [10,14] is a natural setting for the large-scale application of discrete domes, while more compliant analogs have promising applications at smaller scales. For instance, discrete structures are used in soft electronics [15], stents [16], and deployable micro-devices [17–19]. It is challenging to predict the mechanical response of discrete domes to external loading [20,21], in particular, because they are prone to catastrophic snap-through instabilities [22,23], not unlike continuous doubly curved shells [24]. Computationally, continuous [25] and element-based [26,27] numerical schemes, combined with group theory [28], have been used to analyze the buckling threshold and post-buckling behavior of discrete domes. Experimentally, most studies have focused on the critical load to failure [29,30], and post-buckling analyses remain scarce [31]. By contrast to the abundant literature on discrete domes, even fewer studies [32] have considered the mechanics of woven domes; predicting both their post-buckling behavior and the stability landscape remain open challenges.

Here, we investigate the post-buckling response of shallow woven domes to indentation, with the possibility of bistability. Our study combines model experiments, simulations using the finite element method (FEM), geometry, and an elastica-based reduced model. The domes are weaved from flat ribbons in a triaxial pattern with a central pentagon. The rest shape of the domes, characterized by a natural angle and radius, is tuned smoothly

* Corresponding author.
E-mail address: pedro.reis@epfl.ch (P.M. Reis).

[1] Current affiliation: Department of Physics, The University of Tokyo, Tokyo, Japan.

[2] Current affiliation: University of Houston, Architected Intelligent Matter Laboratory, Houston, TX, 77024, United States.

[3] Current affiliation: Keio University, Laboratory for Structural Instabilities in Geometry and Materials, Yokohama, Kanagawa, 2238522, Japan.

https://doi.org/10.1016/j.eml.2023.101968

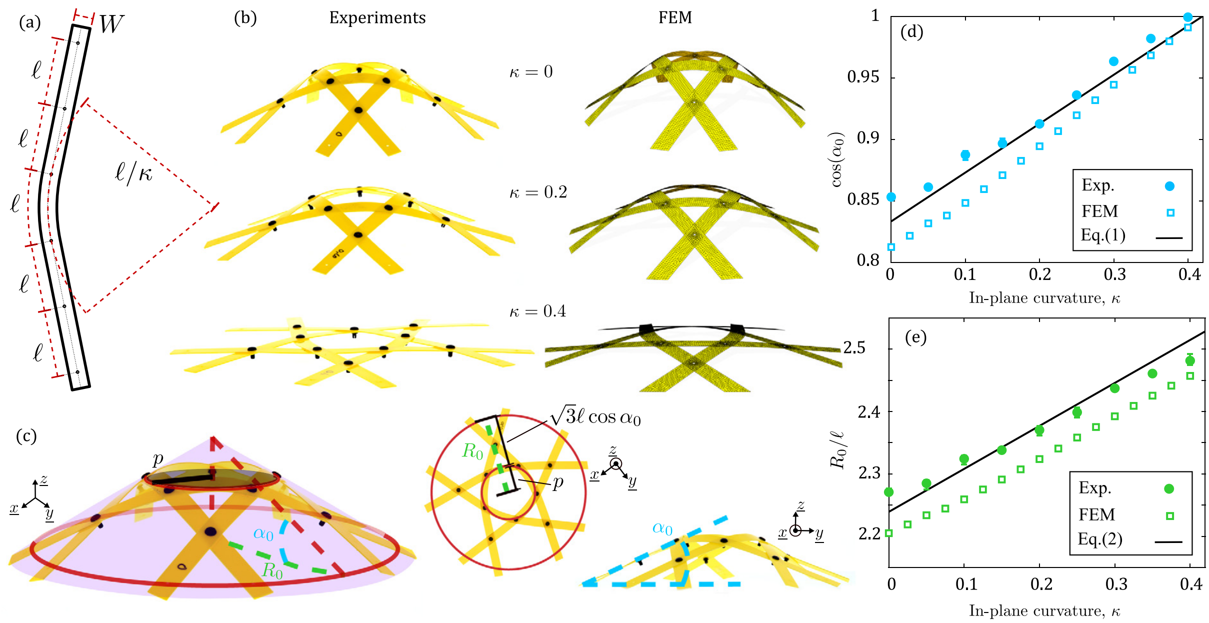

Fig. 1. Rest shape of the woven domes, with varying in-plane curvature of the ribbons. (a) Example of the planar geometry of a curved ribbon with $\kappa = 0.4$. (b) Experimental and FEM-computed rest shapes of woven domes with $\kappa = \{0, 0.2, 0.4\}$. (c) Approximation of the rest shape by a conical surface, with the definition of the rest angle, α_0, and radial extent, R_0, from, respectively, the side and top views, shown here for $\kappa = 0.1$ (d) Rest angle α_0 and (e) radius R_0 of the domes as functions of κ; experiments (circles) and FEM (squares). the experimental error bars represent the minimum and maximum values measured from three realizations. The solid lines in (d) and (e) correspond to the geometric predictions, respectively, from Eqs. (1) and (2).

by varying the in-plane curvature of the constituent ribbons and rationalized by geometrical arguments. Before indentation, the domes are clamped with adjustable boundary conditions, thereby constraining the domes away from their rest shape. Three key design parameters emerge: the in-plane curvature of the ribbons, κ, and the differences, $\Delta\alpha$ and ΔR, of the domes' radii and angles between its rest and constrained shapes, respectively (these quantities will be defined in due course). The clamped domes are loaded with an axially symmetric indentation up to dome inversion, and the resulting mechanical response is characterized for various design parameters. Depending on the values of κ, ΔR, and $\Delta\alpha$, the response can be tuned to switch from monostable to bistable. Finally, we propose a reduced model based on Euler's *elastica* to rationalize the emergence of bistability, capturing the main features of the mechanical behavior of seemingly complex weaves.

2. Realization of the domes: Experiments and FEM

Starting with flat ribbons, the 3D domes are hand-woven into a triaxial weaving pattern [1,2], adopting a technique similar to that developed in Ref. [6]. We use $n = 5$ identical ribbons of width $W = 8$ mm, thickness $h = 0.5$ mm and a total arclength of 150 mm, divided into five segments of equal arclength $\ell = 30$ mm (see Fig. 1a). The ribbons are made of laser-cut polyethylene terephthalate (Plastic Shim Pack DM1210, Partwell Group; Young's modulus $E = 2$ GPa and Poisson's ratio $\nu = 0.35$). Each ribbon contains a middle segment with dimensionless in-plane curvature, κ, such that the centerline there has an arc of radius of curvature ℓ/κ (Fig. 1a). Apart from the middle segment, all others are naturally straight. The value κ is then a direct measure of the angle, in radians, between the two straight portions of the ribbon. The ribbon extremities are extended slightly by $\ell/3$ to enable clamping, but these extensions are not considered in the shape measurements, nor do they play a mechanical role. Weaving is done by sequentially joining the segment ends of matching ribbons and alternating over- and under-crossings. Punctured clearance holes (1.1 mm diameter) at the start and end of each segment serve to install pins (snap rivet, 5.5 mm, polyamide, Distrelec AG, Switzerland) during weaving. The pinned crossings allow for rotation on the tangent plane but constrain position. The ribbons are assembled such that the in-plane curvature of their middle segments points outward of the pentagon. Upon weaving, the layout contains a central pentagon surrounded by outer triangles (see Fig. 1b). A spontaneous 3D shape develops upon assembly, determined by the initial geometry of the ribbons, as we will demonstrate below.

Numerically, the ribbons in the FE model mirror that of the experiments, both in geometry (including the rivet holes) and in material properties. To simulate the weaving process, the ribbons are initially laid flat. Then, for each crossing of the final weave, the corresponding pin holes are linked by fictitious wires whose lengths are incrementally shrunk to zero. Finally, the elements around the pin holes are tied in translation and rotation to the corresponding elements on the matching ribbon. Hence, the simulation neglects the alternating under and over the crossing, as well as potential ribbon–ribbon contacts. Additional details on the FEM simulations are provided in Appendix A.

3. Rest shape of the domes

In the absence of external constraints, the woven ribbons adopt a natural (rest) dome-like shape in the explored range of $0 \leq \kappa \leq 0.4$ [6]. Increasing κ yields shallower domes (Fig. 1b). To quantify the geometry with a reduced number of parameters, we approximate the shape of the structure by a conical surface (Fig. 1c); woven ribbons bend primarily in the direction normal to their plane to span a developable surface [6]. With this conical approximation, only two parameters are needed to quantify the rest shape of the weaves: the radial extent of the cone, R_0, measured from the circle passing by the extremities of the ribbons, and the angle between the horizontal and the slope of the cone, α_0 (Fig. 1c). In Fig. 1(d,e), we plot R_0 and α_0 as functions of κ. In the experiments, α_0 and R_0 are measured through digital photography. In the FEM, α_0 is measured from the slope between the extremities of the ribbons and the pentagonal pins, and R_0 is measured from the coordinates of the extremities of the ribbons.

Towards rationalizing the rest shape of the dome, we assume that pure bending of the ribbons is the only excited deformation mode. Relying on the Gauss–Bonnet theorem [33], previous work [6] has shown that the integral of the Gaussian curvature of the surface enclosed by the tangents of its delimiting polygonal elements is a function of the in-plane curvature of the ribbons: $\mathcal{K}_n = \frac{\pi}{3}\left(6 - n\left(1 + \frac{3}{2\pi}\kappa\right)\right)$, with $n = 5$ for a pentagon. The geometry of a cone provides an alternative expression for the integrated Gaussian curvature as a function of the cone opening angle: $\mathcal{K}_n = 2\pi(1 - \cos\alpha_0)$. Equating these two expressions, the opening angle of the cone can be determined as:

$$\cos\alpha_0 = \frac{n}{6}\left(1 + \frac{3}{2\pi}\kappa\right). \tag{1}$$

The radial extent of the cone, R_0, is the sum of the radius, p, of the circle inscribed by the corners of the pentagon and the length, $\sqrt{3}\ell\cos\alpha_0$, of the projection onto the cone base and in the radial direction, of the segment connecting the pentagon to the cone edge (see Fig. 1c). We approximate the perimeter of the circle inscribed by the pentagon to the perimeter of the pentagon, $2\pi p \approx n\ell$ to obtain:

$$\frac{R_0}{\ell} = \frac{\sqrt{3}n}{6}\left(1 + \frac{3}{2\pi}\kappa\right) + \frac{n}{2\pi}. \tag{2}$$

In Fig. 1(d–e), we compare the experimental and FEM-computed data for $\cos\alpha_0$ and R_0/ℓ versus κ, together with, the linear geometrical predictions of Eq. (1) and Eq. (2), respectively. The agreement is particularly good between the experiments and the geometric predictions. However, there is a systematic offset ($\approx -5\%$) for the FEM data. We attribute this discrepancy to the over-simplification of the modeling of the pinning conditions at the crossings. While in FEM, these crossings are constrained to be strictly co-planar, in the physical samples, the pins may not completely hinder rotation. The importance of this discrepancy in the mechanical response is alleviated by the clamping conditions imposed on the rest shape.

4. Clamping of the domes and design parameter space

Having used geometric arguments to characterize the rest shape of the domes, we proceed by describing how the boundary conditions (BCs) are set before indentation. The domes are clamped by their ribbons' ends in a way that imposes their initial angle α (Fig. 2a) and radial extent R (Fig. 2b). Experimentally, this clamping is done using acrylic plates, whose angles and radial position can be varied continuously (Fig. 2c, inset), with a precision of ± 0.05 rad. for α and ± 0.5 mm for R. In FEM, the corresponding displacements and rotations are imposed at the ribbons' ends. The resulting clamped shape is then a compromise between the rest shape imposed by the weaving pattern and the external BCs. Through the conical approximation, the imposed angle α and radial extent R of the clamped shapes can be directly compared to the corresponding values at rest (before clamping), α_0 and R_0, by their differences $\Delta R = (R - R_0)/\ell$ and $\Delta\alpha = \alpha - \alpha_0$. Positive (negative) values of ΔR and $\Delta\alpha$ correspond to a radially stretched (compressed) dome. Together with the in-plane curvature of the ribbons, κ, there are three design parameters $(\kappa, \Delta R, \Delta\alpha)$, which can be varied independently and continuously to shape the domes before indentation.

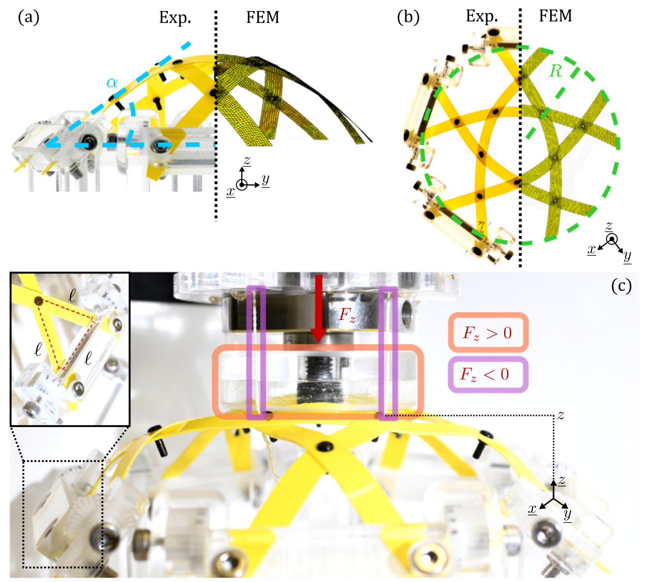

Fig. 2. Domes clamping and indentation method. Side view (a) and top view (b) of a representative clamped dome ($\kappa = 0.1$, experiments on the left, FEM on the right), with an external angle $\alpha = 0.873$ rad. (a) and radius $R = 63$ mm (b) imposed to the outer part of the dome. (c) Indentation is imposed by an acrylic ring (in orange) when $F_z > 0$ and inextensible threads (in purple) when $F_z < 0$. Zoom inset is a close-up of the clamping mechanism. (For interpretation of the references to color in this figure legend, the reader is referred to the web version of this article.)

5. Response of the domes to mechanical indentation

The domes are loaded by imposing the vertical position, z, of the pins associated with the pentagon. In the experiments, a rigid acrylic ring of inner radius 23.5 mm ($\approx p$) and thickness 4 mm, pushes the pins downward (see orange highlight in Fig. 2c) and the vertical force, F_z, is recorded (Instron 5943, 1 kN load cell). To access negative values of F_z, inextensible cables (see purple highlights in Fig. 2c) connect the pin holes to a second rigid plate set above the pushing ring. The length of the cables is set so that they are only in tension when $F_z < 0$. The smooth transitions at $F_z = 0$ in the experimental data (Fig. 3) validate this indentation method (the results are discussed in detail below). Despite discrete domes being known to display complex indentation responses because of asymmetric configurations [31], by pushing/pulling on all the pins of the central pentagon simultaneously, our method favors n-fold symmetric modes of deformation. The indentation rate is 1 mm/s, slower than the snapping timescale ($\approx$ 50 ms); hence, the experiments can be considered quasi-static.

In FEM, the vertical displacement z is imposed on the nodes around the corresponding pin holes; all other degrees of freedom (translational or rotational) are set free. The total reaction force F_z is extracted as the resultant of the vertical reaction forces of all the affected nodes.

In Fig. 3, we plot a representative example of $F_z(z)$ for a dome with $(\kappa, \Delta R, \Delta\alpha) = (0.1, -0.21, 0.37\,\text{rad.})$, see also corresponding video in Appendix C. The origin $z = 0$ is set on the x–y plane of the clamps, and the initial value z_A measures the height of the clamped dome before indentation. Indentation corresponds to decreasing z from z_A, and inverted configurations with pentagonal pins below the clamping plane have $z < 0$. The experiments and FEM results exhibit qualitatively similar features, marked $A, B, \ldots, E$ in Fig. 3. Each feature is associated with a corresponding FEM snapshot. Starting from an initial stable shape (A), the force quickly increases to a maximum (B). Then, the decreasing force is interrupted by a sudden drop $C - D$ at a

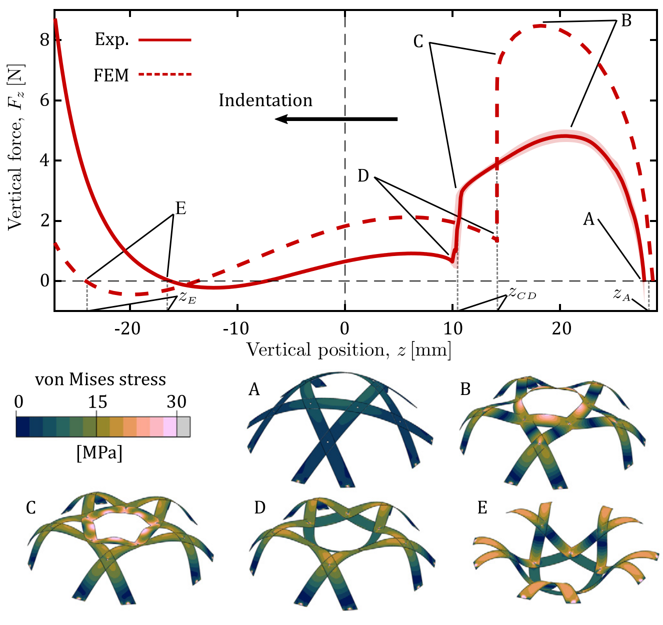

Fig. 3. Representative indentation response of a weaved dome with $k = 0.1$, $\Delta R = -0.21$ and $\Delta\alpha = 0.37$. (Top) The experimental response over 5 runs is represented by the average (solid red curve) and minimum, and maximum values reached (shaded region). The dashed red curve is the corresponding FEM simulation for the same parameters. (Bottom) The FEM snapshots (A to E), colored by the von-Mises stress of the elements, illustrate the main features of the response. (For interpretation of the references to color in this figure legend, the reader is referred to the web version of this article.)

position z_{CD}, triggered by the snap-through inversion of the segments belonging to the central pentagon. Past a second smaller local maximum, F_z decreases gradually to negative values before turning around and diverging upward. Point E, where $F_z(z_E) = 0$ and $\mathrm{d}F_z/\mathrm{d}z|_{z_E} < 0$, corresponds to a second (inverted) stable state. The FEM snapshots, colored by the von Mises stress of the elements, show that most of the deformation occurs at the segments outside the pentagon; the central segments accumulate stress without barely deforming, except during the snap-through inversion at $C-D$. Despite the overall qualitative agreement between experiments and FEM, there are quantitative mismatches in the force magnitudes and the exact indentation positions of the main features (*e.g.*, z_{CD} and z_E). We speculate that these discrepancies may arise because, in the FEM model, the ribbon–ribbon intersections at the crossing points are implemented by idealized kinematic conditions and not by a direct representation of the physical pins in the experiments. This difference could potentially impose more rigid conditions (whereas, in the experiments, there is some compliance, even if small, due to the clearance in the pin holes) and the different loading methods (no indentor-pins contact in FEM).

We proceed by systematically exploring the design parameter space: in-plane curvature, radius difference, and angle difference, $(\kappa, \Delta R, \Delta\alpha)$, in the neighborhood of the representative case with $(0.1, -0.21, 0.37)$. In Fig. 4, we plot $F_z(z)$ for both experiments (Fig. 4a1, b1, c1) and FEM (Fig. 4a2, b2, c2). With the caveat mentioned above for the quantitative discrepancies between experiments and simulations, we focus on the trends of how the three design parameters tune the characteristics of the response to indentation. The height of the initial state, z_A, and the maximum force at B (see Fig. 3) are reduced with κ (Fig. 4a1, a2) or ΔR (Fig. 4b1, 2), while $\Delta\alpha$, (Fig. 4c1, 2) has little influence over them. The position, z_{CD}, of the snap-through inversion is only marginally sensitive to $\Delta\alpha$ and κ. However, increasing κ reduces the relative position between the start of indentation and the inversion point, $z_A - z_{CD}$. For $\kappa = 0.4$, the rest dome is nearly flat before clamping, and there is no snap-through. By contrast, $z_A - z_{CD}$ remains constant with increasing ΔR, but z_{CD} decreases progressively towards 0. For $\Delta R \gtrsim 0$, and $\Delta\alpha = -0.51$, z_{CD} suddenly jumps to negative values beyond the force minima. Finally, pre-stressing the dome by increasing ΔR or $\Delta\alpha$ lifts all minima progressively, up to a point where $F_z > 0$ for the entire indentation range and the domes lose their second (inverted) stable state. Varying κ only alters this bistability marginally.

This exploration of the design space highlights the tunable indentation response of woven domes. Particular rays in this parameter space modify some of the response features while keeping others untouched. For example, increasing $\Delta\alpha$ changes the bistability but barely influences the first force maximum and snap-through inversion. By contrast, κ has little influence on bistability but affects the maximal force significantly.

6. *Elastica*-based reduced model for the stability landscape

Next, we propose an *elastica*-based approximation to rationalize the conditions for bistable or monostable behavior of the woven domes, seeking to compare the stability criteria of the physical system to predictions from this simplified model.

From the snapshots in Fig. 3, we observe that, away from snap-through, the central pentagonal region undergoes minimal deformation during indentation; most of the deformation is taken by the external triangles. The deformation is predominantly in bending, orthogonally to the plane of the ribbons, while their centerlines remain mostly confined to the plane $(\underline{\mathbf{e}}, \underline{\mathbf{z}})$ (see Fig. 5a1). These observations suggest that some of the mechanical features of the segments between the inner polygon and the clamps should be captured by identical and independent *elastica* curves (pink curves in Fig. 5a1), while the central (nearly rigid) pentagon can be replaced by an effective BC. The proposed construct (Fig. 5a2,3) assumes an inextensible elastic curve parametrized by an effective arclength $S \in [0..L]$, evolving in the $(\underline{\mathbf{e}}, \underline{\mathbf{z}})$ plane, and with bending stiffness $D = EWh^3/12(1-\nu^2)$. The two ends are assumed clamped, imposing: the start and end angles ($\tilde{\alpha}_0$ and $\tilde{\alpha}$, respectively), the height difference (z), and the projected distance between the ends (U); these constraints, expressed using the domes' parameters, are $\sin\tilde{\alpha}_0 \equiv \sin\alpha_0\cos(\pi/6)$, $\sin\tilde{\alpha} \equiv \sin\alpha\cos(\pi/6)$, and $U = \sqrt{(R-p)^2 + \ell^2}$ is assumed constant upon indentation and follows the geometrical approximation shown in Fig. 5(a2). For a set of in-plane curvature κ, BCs (R, α) and indentation z, the *elastica* is solved for its shape and the vertical force exerted on $S = 0$. The total indentation force, F_z, is then computed as the resultant of the $2n$ *elasticas*. (See Appendix B for a more detailed description of the geometry and the solution method.)

Fig. 5(b) presents *elastica* predictions (dotted line) compared to experiments (solid line), for the representative case with $(\kappa, \Delta R, \Delta\alpha) = (0.1, -0.21, 0.37)$. The sensitivity of the model is conveyed by the shaded regions representing variations of the total effective arclength L by $\pm 1\%$ (dark pink) and $\pm 3\%$ (light pink). The snap-through inversion is interpreted as a change of the BCs at $S = 0$, from $+\tilde{\alpha}_0$ to $-\tilde{\alpha}_0$, but the prediction of this instability is out of reach of the *elastica* approximation. This inversion involves snapping of the ribbons of the pentagon under coupled forces and moments from the external triangles and would require a more sophisticated model than the *elastica* to be predicted. The pre- and post-inversion responses are then estimated independently by changing this BC. The *elastica* model qualitatively recovers many of the observed features, including the first maximum and the inverted stable state. Comparing the resulting centerline shapes against the ones measured by FEM

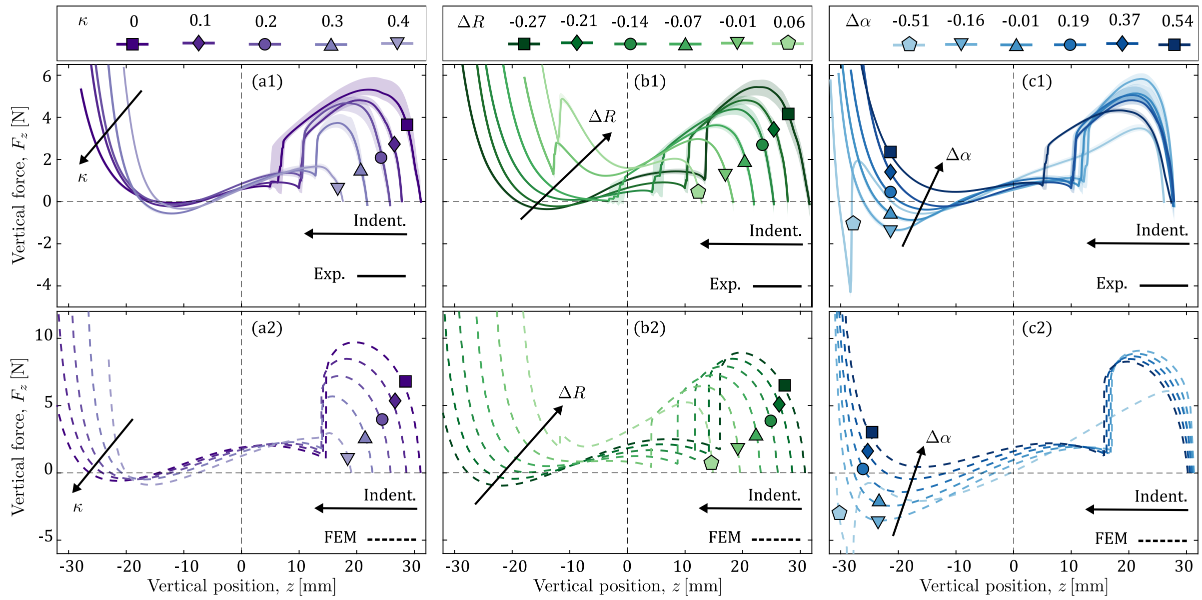

Fig. 4. Systematic exploration of the effects of κ, ΔR, and $\Delta\alpha$ on the indentation response. Top panels (a1, b1, c1, solid lines) for experiments and bottom panels (a2, b2, c2, dashed lines) for FEM. (a) Fixed $\Delta R = -0.21$ and $\Delta\alpha = 0.37$, varying $0 < \kappa < 0.4$. (b) Fixed $\kappa = 0.1$ and $\Delta\alpha = 0.37$, and varying $-0.27 < \Delta R < 0.06$. (c) Fixed $\kappa = 0.1$ and $\Delta R = -0.21$, and varying $-0.51 < \Delta\alpha < 0.54$. For the experimental data (solid curves), the shaded regions correspond to minimum/maximum reached over 5 runs.

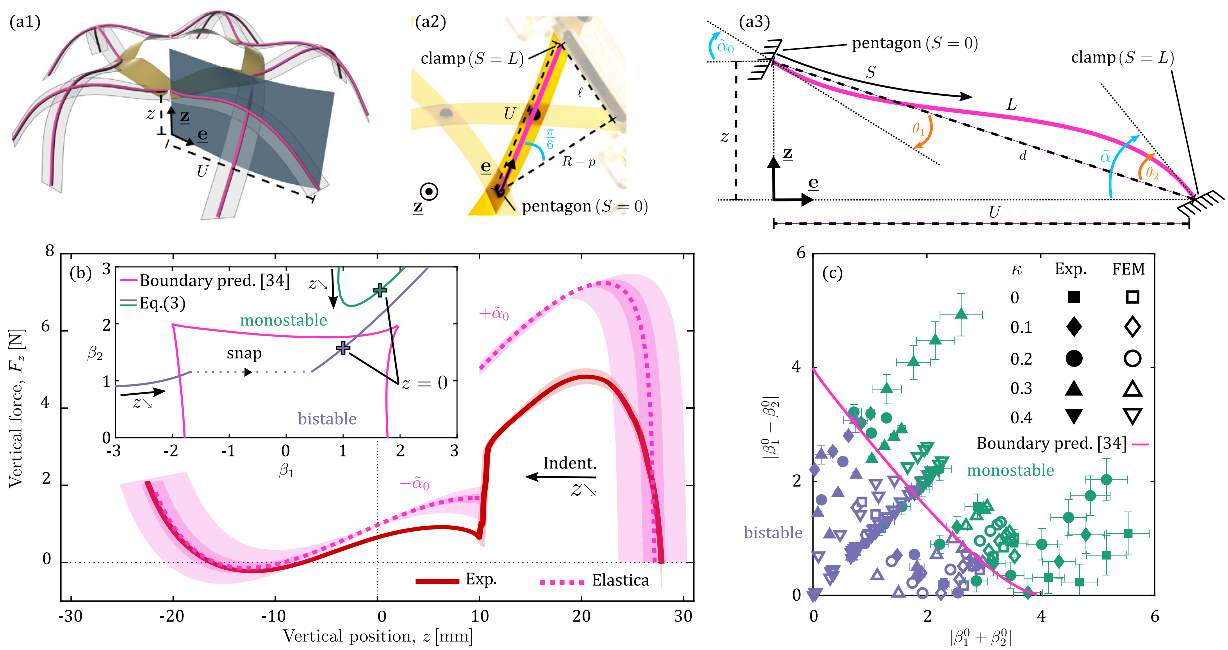

Fig. 5. *Elastica* approximation and stability diagram. (a1) 3D schematic from FEM highlighting the segments in the sample that are modeled as *elasticas* (pink) or as rigid segments (yellow), the latter corresponding to the central pentagon. (a2) Top view and (a3) equivalent side-view schematic (on the $\underline{\mathbf{e}}, \underline{\mathbf{z}}$ plane) of the *elastica*. (b) Indentation response of the $(\kappa, \Delta R, \Delta\alpha) = (0.1, -0.21, 0.37)$ dome: experiments (solid red line) and *elastica* model (dotted pink line). The dark and light, shaded regions represent the uncertainties in the *elastica* prediction associated with varying L by $\pm 1\%$ and $\pm 3\%$ respectively. Inset, trajectories in the (β_1, β_2) plane for the indentation of two domes ($(\kappa, \Delta\alpha) = (0.1, 0.37)$): one bistable ($\Delta R = -0.27$, purple), one monostable ($\Delta R = -0.01$, green); the crosses mark the associated $z = 0$ point. The predicted curve [34] for the bistability-monostability boundary is drawn in pink. (c) Stability diagram in the $(|\beta_1^0 - \beta_2^0|, |\beta_1^0 + \beta_2^0|)$ parameter space with the predicted phase boundary (pink). The symbols for the monostable (green) and bistable (purple symbols) configurations correspond to experiments (closed symbols) and FEM (open symbols). Error bars are $\pm 1\%$ variations of L. (For interpretation of the references to color in this figure legend, the reader is referred to the web version of this article.)

also shows good agreement (Fig. B.7), confirming that the central pentagon acts as a rigid BC for the external triangles. However, similarly to FEM and for similar expected reasons, it overestimates F_z, especially for the maximum value. Also, the *elastica* is sensitive to the input parameters (*e.g.*, L) that approximate the dome geometry (see shaded regions in Fig. 5b). In any case, this reduced model does recover the second inverted stable state (minimum), suggesting that the framework is valuable to gain insight into the dome stability.

We will now assess to what extent the number of stable states allowed by the *elastica* reduction informs on the stable configurations reached by the dome upon indentation. The stability of clamped–clamped *elastica* has been analyzed thoroughly in the past [34–36]. Here, we follow the modeling framework and notation of Wan et al. [34], which, for convenience, is briefly overviewed next. A clamped–clamped *elastica* admits either one or two stable states, depending on its BCs. From the dimensionless governing equations, the following two stability-controlling parameters emerge:

$$\beta_1 = \sin\theta_1\sqrt{\frac{L}{L-d}}, \qquad \beta_2 = \sin\theta_2\sqrt{\frac{L}{L-d}}, \tag{3}$$

where L is the total effective arclength of the *elastica* and, in terms of the geometry of the woven domes, $d = \sqrt{U^2+z^2}$ is the distance between clamps, and the imposed angles at the extremities are $\theta_1 = \pm\tilde{\alpha}_0 - \arctan(z/U)$ and $\theta_2 = \tilde{\alpha} - \arctan(z/U)$ (see Fig. 5a3). The $\pm$ sign in θ_1 denotes the *elastica* solution for pre snap-through ($+\tilde{\alpha}_0$ imposed at $S = 0$, hence a + sign) or post snap-through ($-\tilde{\alpha}_0$ imposed at $S = 0$, hence a - sign). These parameters reflect the relative strength of the angular (θ_1, θ_2) and confinement ($L - d$) constraints imposed between the two ends of the *elastica* [35].

Wan et al. [34] showed that a clamped–clamped *elastica* is bistable (or monostable) inside (or outside) a closed region centered around $(\beta_1, \beta_2) = (0, 0)$. However, in our case, β_1 and β_2 are functions of the indentation z. As such, our dome is not characterized by a single point in the (β_1, β_2) space but, instead, by a z-parametrized trajectory. Analogously to doubly curved continuous shells, the indentation can give access to different stable states [37]. In the inset of Fig. 5(b), we show the trajectories of two configurations, one monostable ($(\kappa, \Delta R, \Delta\alpha) = (0.1, -0.01, 0.37)$, in green), and one bistable ($(0.1, -0.27, 0.37)$, in purple). In the latter, there is a trajectory jump related to the sign change in θ_1 before and after snap-through. The trajectory for the monostable dome stays outside of the bistability boundary (pink line), whereas the bistable dome crosses through into it, suggesting a strong relation between the number of stable configurations of the domes and *elastica* bistability.

Next, we validate the above *elastica* scenario over a wide range of parameters, seeking to obtain a unique bistability criterion for our system by considering a single point within the trajectory, (β_1^0, β_2^0). We pick $z = 0$ (shown by the '*plus*' signs in the inset of Fig. 5b) because it is nearly equidistant to the two stable configurations. Moreover, this choice facilitates interpretation by yielding simple expressions for β_1 and β_2 as functions of $\Delta\alpha$, ΔR, and κ. In the (β_1, β_2) space, the axes $\beta_1 + \beta_2 = 0$ and $\beta_1 - \beta_2 = 0$ are symmetry axes of the bistable region, and there is no detriment in presenting the results in the simpler $(|\beta_1 - \beta_2|, |\beta_1 + \beta_2|)$ parameter space.

The stability experiments and FEM simulations are carried out by systematically varying $(\kappa, \Delta R, \Delta\alpha)$, for a more comprehensive set of parameters than the representative cases shown in Fig. 4, and attesting the bistability of the dome through the presence of a point in the $F_z(z)$ indentation curve with $F_z = 0$ and $\frac{dF_z}{dz} < 0$. For the geometry of each configuration, we evaluated Eq. (3) with $z = 0$, to obtain a location in the $(|\beta_1^0 - \beta_2^0|, |\beta_1^0 + \beta_2^0|)$ space. In the phase diagram shown in Fig. 5(c), the bistable (and the monostable) domes are represented by the purple (and the green) symbols (, respectively); the experimental (and FEM-computed) data is represented by the closed (and open) symbols (, respectively). The configurations showing more than two stable states are also represented in purple. The stability-boundary curve (pink solid line) obtained from the *elastica* analysis [34] predicts the monostability-to-bistability transition region observed in the experiments and FEM remarkably well. However, determining the exact nature of the relationship between the (β_1, β_2) trajectory upon indentation and the existence of stable configurations of the domes remains an open question.

To establish a link between the above findings and the data in Fig. 4, we express the stability parameters $|\beta_1^0 - \beta_2^0|$ and $|\beta_1^0 + \beta_2^0|$ as functions of κ, ΔR and $\Delta\alpha$. We take the limits of small angles ($\alpha \ll 1$, $\alpha_0 \ll 1$), barely curved ribbons ($\kappa \ll 1$), and BCs close to the natural shape ($\Delta R \ll 1$, $\Delta\alpha \ll 1$). Expanded to first order, the expressions simplify to $|\beta_1^0 - \beta_2^0| \sim |\Delta\alpha|$ and $|\beta_1^0 + \beta_2^0| \sim |1 + a\Delta\alpha + b\Delta R - c\kappa|$, with positive constants a, b, c of order 1. Pre-stressing the dome by increasing $\Delta\alpha$ (or ΔR) causes $|\beta_1^0 - \beta_2^0|$ and $|\beta_1^0 + \beta_2^0|$ to deviate from 0, with the possibility of the values passing through the bistability-monostability boundary. When that happens, the dome ceases to exhibit bistable behavior, consistently with the experimental observations. By contrast, increasing κ decreases $|\beta_1^0 + \beta_2^0|$ while not modifying $|\beta_1^0 - \beta_2^0|$ to first order. In that case, if the dome were already in the bistability region for $\kappa = 0$, then it would remain bistable. Overall, the *elastica*-based reduced model enables us to rationalize many features of the behavior of our woven domes, in particular, providing predictions for their stability landscape given a set of design parameters $(\kappa, \Delta R, \Delta\alpha)$.

7. Conclusions

The present work recognizes woven domes as a new class of discrete domes offering an interesting alternative to more classic architectures [31]. We found that the indentation response of woven domes features highly nonlinear behavior, including force maximum, snap-through inversion, and bistability. These features can be tuned smoothly by adjusting the rest shape and BCs of the dome and are captured by the FEM simulations semi-quantitatively. Furthermore, a clamped–clamped *elastica*-based model successfully predicts the parameter space and the associated boundary between monostable and bistable behavior. The cross-sectional asymmetry of the constituent ribbons (here a ratio of 16 to 1 between the width and the thickness) enforces bending to a single plane, which may enhance reproducibility and reduce the complexity of possible configurations when compared to domes made out of beams with more symmetric cross-sections, such as rectangular [14,30] or circular [29]. This asymmetry also enables continuous tuning of the dome's rest shape with a single parameter κ, which, together with the boundary parameters $(\Delta R, \Delta\alpha)$, offer a rich design space.

As in other types of discrete domes [29], a detailed description of the joints is required for quantitative predictions of the indentation response. To enable the accurate predictive design of woven domes using FEM simulations, further work is needed in modeling the specifics of the crossing points, including taking into account the over- and under-passing and the frictional contact between ribbons. Still, we highlight the prominence of geometry in 3D woven domes, and hence the scalability of the underlying mechanism, together with the rich design space, with the possibility of robust tuning of the response. Together, these features suggest an enticing potential for applications, from large architectural structures to micro-scale devices, well beyond the traditional craft that motivated our study.

Declaration of competing interest

The authors declare that they have no known competing financial interests or personal relationships that could have appeared to influence the work reported in this paper.

Data availability

Data will be made available on request.

Acknowledgments

The authors thank Guangchao Wan for providing the prediction data of [34] for Fig. 5. Samuel Poincloux acknowledges the financial support from the Japanese Society for the Promotion of Science as a JSPS International Research Fellow.

Appendix A. Finite element simulations

A multi-step finite element (FE) simulation procedure is implemented using the commercial software package ABAQUS 6.14 to gain deeper insight into the underlying phenomena and expand the parameter space of the exploration. Each FE model consists of $n = 5$ number of identical ribbons placed around the origin. The geometry of the ribbons in each FE model (Fig. A.6a) mirrors that of the experiments, as described in Section 2, and is parametrized by the in-plane curvature of the middle segment, κ. The holes that accommodate the snap rivets in the experiments are included in the FE geometry. At the crossings, the snap rivets force the two overlapping ribbons to be co-planar, a condition that is enforced for both the inner and the outer pin pairs throughout the FE simulations. The ribbons are meshed using quadratic shell elements (S8R). Following a mesh sensitivity analysis, each ribbon is assigned eight elements width-wise, leading to approximately 1600 elements per ribbon.

Three quasi-static simulation steps are performed sequentially to the aforementioned model, considering geometric nonlinearity throughout. *Step 1:* The ribbons are weaved to attain the natural rest shape using the technique first proposed in Ref. [6]. Here, we restricted our study to rest shapes with a positive integrated Gaussian curvature. In these dome-shaped geometries, we can impose the BCs such that the end of the ribbons (indicated as boundary edges in Fig. A.6a) do not move in the vertical direction, *i.e.* $z = 0$ during weaving. Weaving is performed by incrementally reducing to 0 the distances between the neighboring outer pins. In the FE model, this is implemented by shrinking the wires as indicated in Fig. A.6b. Note that these zero-length constraints are propagated to the next simulation steps to maintain the woven shape. *Step 2:* The prescribed BCs are imposed on the natural rest shape in accordance with the experimental setup described in Section 4. The prescribed radial displacements, ΔR, are imposed on the translational degrees of freedom (DOFs) of the boundary nodes (Fig. A.6c), moving them towards, or away, from the origin. The prescribed rotations are imposed on the in-plane rotational DOFs of the same set of nodes. Rotation with respect to the z-axis remains unconstrained. *Step 3:* Having prescribed the BCs, an indentation is applied as a vertically-downward incremental displacement on the inner ring of pins (Fig. A.6d), with a magnitude of $-2z_{\max}$, where $z_{\max}$ is the initial height of the inner pins after clamping. For models featuring an inversion of the inner polygon, we assign a dissipated energy fraction of 0.0002 and a maximum ratio of stabilization to strain energy of 0.05 to facilitate convergence during snap-through.

Compared to the experiments, the FE simulations provide a vaster access to the parameter space, with the enlarged feasible set of values of κ, ΔR, and $\Delta\alpha$, but also an estimation of the deformation fields in the ribbons upon indentation. The geometric parameters z, U, α, L, and R are extracted directly from the simulations and used to compute the FEM quantities in Fig. 5.

Appendix B. More details of the *elastica* model in Section 6

The woven dome comprises $n = 5$ ribbons, each of which is further divided into three parts. In our *elastica* framework, the central segment is modeled as an effective rigid boundary, while the first and last segments are considered as two independent *elasticas*, such that a dome contains $2n = 10$ identical *elasticas*.

The *elastica* approximation is computed in the frame ($\underline{\mathbf{e}}$, $\underline{\mathbf{z}}$) (Fig. 5a), with the ribbons assumed inextensible, and the centerline restricted to deform in the vertical plane (Fig. 5a1). The arclength S starts at the crossing with the inner pentagon ($S = 0$), and ends at the acrylic clamps ($S = L$), as shown in Fig. 5(a2). While the *elastica* consists of two segments of arclength ℓ, the total arclength L is an effective length because of the finite width of the ribbons and the effective-clamp approximation at $S = 0$. We define $L = (2 - \varepsilon)\ell$, where $\varepsilon = 0.067$ is a small and positive unknown parameter determined by fitting the response around the second stable state (yielding $L = 58$ mm). Even if this correction seems small, the indentation response is sensitive to the value of L, as illustrated in Fig. 5(b) by the shaded (pink) regions surrounding the elastica prediction, whose extent corresponds to variations in L by $\pm 1\%$ and $\pm 3\%$ (dark and light shades, respectively).

At $S = L$, the BC is assumed naturally clamped, as in the experiments. At $S = 0$, given that the central segment is considered rigid away from the snap-through region, the BC is regarded as an effective clamp (Fig. 5a3). These BCs impose the initial and final positions and angles of the *elastica*. The external clamps impose an angle α in the radial direction of the dome, but the plane ($\underline{\mathbf{e}}$, $\underline{\mathbf{z}}$) of the *elastica* makes an angle $\pi/6$ with respect to this radial direction (Fig. 5a2). This angle of $\pi/6$ is imposed by the weaving pattern, and then enforced in the same plane as the centerline of the ribbon. Hence, at $S = L$, the imposed angle $\tilde{\alpha}$ is $\sin\tilde{\alpha} \equiv \sin\alpha\cos(\pi/6)$. At $S = 0$, the rigid segments remain in the same shape of the rest dome, thus imposing an angle α_0 in the radial direction and translating into the angle $\tilde{\alpha}_0$ with $\sin\tilde{\alpha}_0 \equiv \sin\alpha_0\cos(\pi/6)$ in the ($\underline{\mathbf{e}}$, $\underline{\mathbf{z}}$) plane of the *elastica*. The distance separating the two ends, projected on a plane perpendicular to the indentation direction $\underline{\mathbf{z}}$, is denoted by U and is assumed constant. This quantity is directly linked to the imposed radius R, the radial extent of the pentagon $p = n\ell/2\pi$, and the segment length ℓ: $U = \sqrt{(R-p)^2 + \ell^2}$.

Within an *elastica* framework, the positions of the centerline are given by $u(S)\underline{\mathbf{e}} + w(S)\underline{\mathbf{z}}$, and $\gamma(S)$ is the tangent angle. The Cartesian coordinates and the tangent angle are linked by the following relations: $u(S) = \int_0^S \cos(\gamma(\tilde{S}))\mathrm{d}\tilde{S}$ and $w(S) = \int_0^S \sin(\gamma(\tilde{S}))\mathrm{d}\tilde{S}$. At equilibrium, the *elastica* must satisfy the ordinary differential equation:

$$D\ddot{\gamma} + f_e \sin\gamma - f_z \cos\gamma = 0, \tag{B.1}$$

where D is the ribbons' bending stiffness, and the differentiation $\dot{(\ )} = \mathrm{d}/\mathrm{d}S$ is with respect to arclength. The unknown internal forces, horizontal (f_e) and vertical (f_z), are constant and defined positive in the $+\underline{\mathbf{e}}$ and $-\underline{\mathbf{z}}$ direction, respectively. Before snap-through, the clamped BCs at $S = 0$ are $\gamma = \tilde{\alpha}_0$, $u = 0$, $w = z$. At $S = L$, $\gamma = \tilde{\alpha}$, $u = U$ and $w = 0$. Past snap-through, the only modified BC is $\gamma(S = 0) = -\tilde{\alpha}_0$. Eq. (B.1) is solved numerically using a shooting method: integrating Eq. (B.1) from $S = 0$ with an initial guess of $(\dot{\gamma}, f_e, f_z)$; these parameters are then varied following a gradient descent (`fsolve` in Matlab R2020b), until satisfying the expected BCs at $S = L$.

For a given indentation z, solving the *elastica* yields the centerline position and the internal forces, of which f_z is of particular interest. To obtain the full indentation response, the $F_z(z)$ curve plotted in Fig. 5(b), the *elastica* is solved for decreasing values of $w(S = 0) = z$, with $\gamma(s = 0) = \tilde{\alpha}_0$ *before* snap-through ($z < z_{CD}$) and $\gamma(s = 0) = -\tilde{\alpha}_0$ *after* snap-through ($z > z_{CD}$). Since the dome is composed of $2n = 10$ independent *elasticas*, the indentation response is the resultant $F_z(z) = 10f_z(z)$. Examples of the resulting centerline shapes and tangent angle profiles $\gamma(S)$ are plotted in Fig. B.7 for selected indentations.

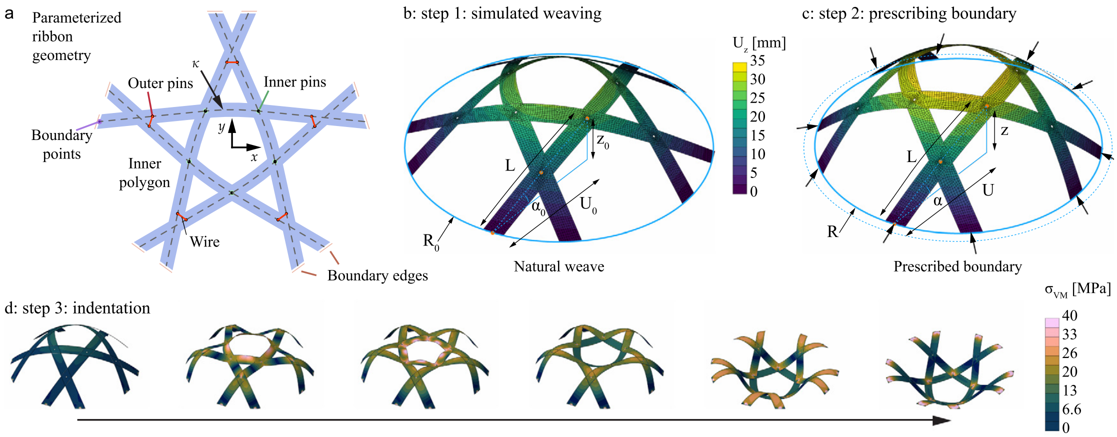

Fig. A.6. Framework and results for the FEM simulations. (a) Set up of the initial ribbon geometry, (b) *Step 1* of the simulations: weaving the dome structure to its natural rest shape, (c) *Step 2* of the simulations: imposing prescribed displacements and rotations at the boundary, (d) *Step 3* of the simulations: indentation of the inner polygon with a prescribed vertical displacement.

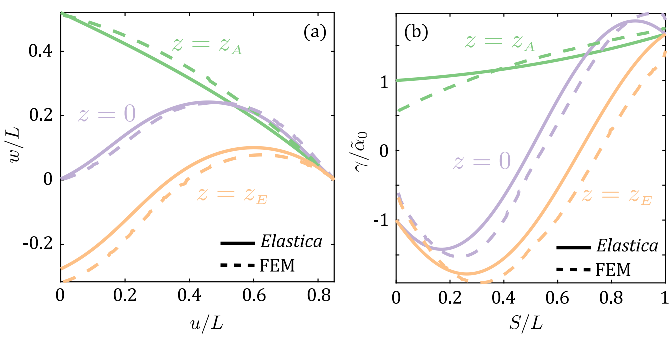

Fig. B.7. (a) Predicted shapes for the external triangle in the ($\underline{\mathbf{e}}$, $\underline{\mathbf{z}}$) plane, obtained from the FEM simulations (dashed lines) and the *elastica* model (solid lines), as quantified by the deformation of the centerline. Three stages of indentation are considered: one before snap-through (at $z = z_A$) and the other two after snap-through (at $z = 0$ and z_E), represented by the green, purple, and orange lines, respectively. (b) Corresponding variation of the tangent angle, γ, along the arclength, S, rescaled by the angle $\pm\tilde{\alpha}_0$ imposed at $S = 0$ in the *elastica* model. The parameters of the weaved dome are $(\kappa, \Delta R, \Delta\alpha) = (0.1, -0.21, 0.37)$. (For interpretation of the references to color in this figure legend, the reader is referred to the web version of this article.)

Appendix C. Supplementary data

Video S1. Video (left panel) of the experimental indentation of a clamped weaved dome with (right panel) the corresponding mechanical response. The video is shown for the representative case shown in Fig. 3 with parameters $(\kappa, \Delta R, \Delta\alpha) = (0.1, -0.21, 0.37\,\text{rad.})$. The video is sped up by a factor of 4 (the real indentation speed is 1 mm/s), except near the snap-through, where the video is slowed down by a factor of 2.

Supplementary material related to this article can be found online at https://doi.org/10.1016/j.eml.2023.101968.

References

[1] A.G. Martin, A basketmaker's approach to structural morphology, in: Proc. IASS Annu. Symp., 2015, (29) Int. Assoc. Shell Spatial Struct., 2015, pp. 1–8.
[2] P. Ayres, A.G. Martin, M. Zwierzycki, Beyond the Basket Case: a principled approach to the modelling of Kagome weave patterns for the fabrication of interlaced lattice structures using straight strips, in: Adv. Arch. Geom. 2018, Chalmers University of Technology, 2018, pp. 72–93.
[3] J. Vekhter, J. Zhuo, L.F.G. Fandino, Q. Huang, E. Vouga, Weaving geodesic foliations, ACM Trans. Graph. 38 (4) (2019) 1–22, http://dx.doi.org/10.1145/3306346.3323043.
[4] U. Lewandowska, W. Zajaczkowski, S. Corra, J. Tanabe, R. Borrmann, E.M. Benetti, S. Stappert, K. Watanabe, N.A. Ochs, R. Schaeublin, et al., A triaxial supramolecular weave, Nature Chem. 9 (11) (2017) 1068–1072, http://dx.doi.org/10.1038/nchem.2823.
[5] S. Rana, R. Fangueiro, Braided Structures and Composites: Production, Properties, Mechanics, and Technical Applications, Vol. 3, CRC Press, 2015.
[6] C. Baek, A.G. Martin, S. Poincloux, T. Chen, P.M. Reis, Smooth triaxial weaving with naturally curved ribbons, Phys. Rev. Lett. 127 (2021) 104301, http://dx.doi.org/10.1103/PhysRevLett.127.104301.
[7] Y. Ren, J. Panetta, T. Chen, F. Isvoranu, S. Poincloux, C. Brandt, A. Martin, M. Pauly, 3D weaving with curved ribbons, ACM Trans. Graph. 40 (4) (2021) 1–15, http://dx.doi.org/10.1145/3450626.3459788.
[8] P. Celli, A. Lamaro, C. McMahan, P. Bordeenithikasem, D. Hofmann, C. Daraio, Compliant morphing structures from twisted bulk metallic glass ribbons, J. Mech. Phys. Solids 145 (2020) 104129, http://dx.doi.org/10.1016/j.jmps.2020.104129.
[9] T. Yu, L. Dreier, F. Marmo, S. Gabriele, S. Parascho, S. Adriaenssens, Numerical modeling of static equilibria and bifurcations in bigons and bigon rings, J. Mech. Phys. Solids 152 (2021) 104459, http://dx.doi.org/10.1016/j.jmps.2021.104459.
[10] Z.S. Makowski, Analysis, Design, and Construction of Braced Domes, Nichols Publishing Company, 1984, http://dx.doi.org/10.1139/l85-113.
[11] T.T. Lan, Space frame structures, Struct. Eng. Handbook 13 (4) (1999).
[12] J. Hennicke, K. Matsushita, F. Otto, K. Sataka, E. Schaur, T. Shirayanagi, G. Gröbner, Grid shells (IL 10), Inst. Lightweight Struct., Stuttgart (1974).
[13] C. Baek, A.O. Sageman-Furnas, M.K. Jawed, P.M. Reis, Form finding in elastic gridshells, Proc. Natl. Acad. Sci. 115 (1) (2018) 75–80, http://dx.doi.org/10.1073/pnas.1713841115.
[14] G. Quinn, C. Gengnagel, A review of elastic grid shells, their erection methods and the potential use of pneumatic formwork, in: Mobile and Rapidly Assembled Struct. IV, Vol. 136 (2014) 129, http://dx.doi.org/10.2495/MAR140111.
[15] Z. Yan, M. Han, Y. Yang, K. Nan, H. Luan, Y. Luo, Y. Zhang, Y. Huang, J.A. Rogers, Deterministic assembly of 3D mesostructures in advanced materials via compressive buckling: A short review of recent progress, Extrem. Mech. Lett. 11 (2017) 96–104, http://dx.doi.org/10.1016/j.eml.2016.12.006.
[16] H. Tomita, T. Higaki, T. Kobayashi, T. Fujii, K. Fujimoto, Stenting for curved lesions using a novel curved balloon: Preliminary experimental study, J. Cardiol. 66 (2) (2015) 120–124, http://dx.doi.org/10.1016/j.jjcc.2014.10.009.
[17] J. Panetta, M. Konaković-Luković, F. Isvoranu, E. Bouleau, M. Pauly, X-shells: A new class of deployable beam structures, ACM Trans. Graph. 38 (4) (2019) 1–15, http://dx.doi.org/10.1145/3306346.3323040.
[18] M. Liu, L. Domino, D. Vella, Tapered elasticæ as a route for axisymmetric morphing structures, Soft Matter 16 (33) (2020) 7739–7750, http://dx.doi.org/10.1039/D0SM00714E.
[19] S. Mhatre, E. Boatti, D. Melancon, A. Zareei, M. Dupont, M. Bechthold, K. Bertoldi, Deployable structures based on buckling of curved beams upon a rotational input, Adv. Funct. Mater. (2021) 2101144, http://dx.doi.org/10.1002/adfm.202101144.
[20] V. Gioncu, Buckling of reticulated shells: state-of-the-art, Int. J. Space Struct. 10 (1) (1995) 1–46, http://dx.doi.org/10.1177/026635119501000101.
[21] T. Bulenda, J. Knippers, Stability of grid shells, Comput. Struct. 79 (12) (2001) 1161–1174, http://dx.doi.org/10.1016/S0045-7949(01)00011-6.

[22] A. Beles, M. Soare, Some observations on the failure of a dome of great span, in: Space Structures, Proc. 1st Int. Conf. Space Struct., University of Surrey, 1966, pp. 419–423.
[23] T.V. Galambos, Guide to Stability Design Criteria for Metal Structures, John Wiley & Sons, 1998.
[24] J.W. Hutchinson, Buckling of spherical shells revisited, Proc. R. Soc. Lond. Ser. A Math. Phys. Eng. Sci. 472 (2195) (2016) 20160577, http://dx.doi.org/10.1098/rspa.2016.0577.
[25] S. Malek, T. Wierzbicki, J. Ochsendorf, Buckling of spherical cap gridshells: A numerical and analytical study revisiting the concept of the equivalent continuum, Eng. Struct. 75 (2014) 288–298, http://dx.doi.org/10.1016/j.engstruct.2014.05.049.
[26] R.H. Plaut, Snap-through of shallow reticulated domes under unilateral displacement control, Int. J. Solids Struct. 148 (2018) 24–34, http://dx.doi.org/10.1016/j.ijsolstr.2017.10.008.
[27] W. Huang, L. Qin, Q. Chen, Numerical exploration on snap buckling of a pre-stressed hemispherical gridshell, J. Appl. Mech. 89 (1) (2021) 011005, http://dx.doi.org/10.1115/1.4052289.
[28] T.J. Healey, A group-theoretic approach to computational bifurcation problems with symmetry, Comput. Methods Appl. Mech. Engrg. 67 (3) (1988) 257–295, http://dx.doi.org/10.1016/0045-7825(88)90049-7.
[29] A. López, I. Puente, M.A. Serna, Numerical model and experimental tests on single-layer latticed domes with semi-rigid joints, Comput. Struct. 85 (7–8) (2007) 360–374, http://dx.doi.org/10.1016/j.compstruc.2006.11.025.
[30] H. Ma, S. Ren, F. Fan, Experimental and numerical research on a new semi-rigid joint for single-layer reticulated structures, Eng. Struct. 126 (2016) 725–738, http://dx.doi.org/10.1016/j.engstruct.2016.08.028.
[31] Y. Guan, L.N. Virgin, D. Helm, Structural behavior of shallow geodesic lattice domes, Int. J. Solids Struct. 155 (2018) 225–239, http://dx.doi.org/10.1016/j.ijsolstr.2018.07.022.
[32] R. Mesnil, C. Douthe, O. Baverel, B. Léger, Linear buckling of quadrangular and kagome gridshells: a comparative assessment, Eng. Struct. 132 (2017) 337–348, http://dx.doi.org/10.1016/j.engstruct.2016.11.039.
[33] J.J. Stoker, Differential Geometry, John Wiley & Sons, New York, 1969.
[34] G. Wan, Y. Liu, Z. Xu, C. Jin, L. Dong, X. Han, J.X. Zhang, Z. Chen, Tunable bistability of a clamped elastic beam, Extrem. Mech. Lett. 34 (2020) 100603, http://dx.doi.org/10.1016/j.eml.2019.100603.
[35] M. Gomez, D.E. Moulton, D. Vella, Critical slowing down in purely elastic 'snap-through' instabilities, Nat. Phys. 13 (2) (2017) 142–145, http://dx.doi.org/10.1038/nphys3915.
[36] T.G. Sano, H. Wada, Snap-buckling in asymmetrically constrained elastic strips, Phys. Rev. E 97 (1) (2018) 013002, http://dx.doi.org/10.1103/PhysRevE.97.013002.
[37] M. Taffetani, X. Jiang, D.P. Holmes, D. Vella, Static bistability of spherical caps, Proc. R. Soc. Lond. Ser. A Math. Phys. Eng. Sci. 474 (2213) (2018) 20170910, http://dx.doi.org/10.1098/rspa.2017.0910.